

In-situ imaging of nucleation and growth of superlattices from nanoscale colloidal nanoparticles

Zuochen Wang^{a,b}, Chang Liu^a, Qian Chen^{a,b,c,d,*}

^a Department of Materials Science and Engineering, University of Illinois, Urbana, IL 61801, United States

^b Materials Research Laboratory, University of Illinois, Urbana, IL 61801, United States

^c Beckman Institute for Advanced Science and Technology, University of Illinois, Urbana, IL 61801, United States

^d Department of Chemistry, University of Illinois, Urbana, IL 61801, United States

ARTICLE INFO

Communicated by James J. De Yoreo

Keywords:

A1. Nucleation

A1. Characterization

A2. Growth from solutions

B1. Nanomaterials

ABSTRACT

Nanoparticle-based superlattices have attracted extensive research efforts due to their versatile composition and packing-dependent optical, magnetic, electronic, catalytic, mechanical properties. Yet the experimental understanding of the thermodynamics and pathways of the crystallization processes for these systems, which govern their ultimate morphology, size, and packing structure, has for long remained underexplored. This minireview highlights recent integration of liquid-phase transmission electron microscopy, which allows for real-space, real-time direct imaging of the crystallization processes at the single-particle level, with simulation and the conceptual framework established by pioneers such as Dr. A. A. Chernov. Different aspects of superlattice formation were revealed by direct imaging for the first time, such as the existence of prenucleation precursor in nonclassical crystallization, surface energy-dependent growth, and coalescence, allowing for the charting of phase coordinates and thermodynamic quantities at the nanoscale. We discuss the similarities and differences of crystal growth behaviors in atomic and nanoparticle systems, as well as engineering opportunities to fashion, shape, and achieve quality control in superlattice formation from nanoparticles, for next-generation optical and mechanical metamaterials.

1. Introduction

Crystallization, the emergence of order from disordered units, is a ubiquitous process underpinning different fields across the length scales over four orders of magnitude, all the way from atomic to micron-sized building blocks [1–3]. A diversity of concepts have been developed, including step kinetics and defect formation in atomic film epitaxial growth for metallurgy and semiconductor industry [4], ion clustering and electrostatics in mineralization [5], surface patchiness in protein crystals [6], and rules of geometric packing in colloidal physics [7]. These fields study the kinetics and thermodynamics of crystal growth with an emphasis on the length scale that the building blocks fall into, especially on how it is compared to environmental factors such as the size of ions and ligands, interaction range—the distance over which interactions maintain effective—and diffusion (or mass transport) lengths (Fig. 1a–g). For example, for atomic systems, the building blocks can often be modeled as simple spheres where theory has taken the lead in elucidating various kinetic growth modes (e.g., Volmer-Weber, Frank-

van der Merwe, and Stranski-Frastanov) for thin film growth of crystals [8,9], and the surface energies dictating the shape formation of a stand-alone crystal (e.g., Winterbottom construction) [10]. Regarding the molecular building blocks for biomineralization and protein crystallization, they are comparable in size with ions and ligands, so that their shape and surface patchiness (if any) need to be thoroughly taken care of as exemplified by Chernov's seminal work on protein crystallizations [11–13]. For micron-sized colloids, they are large and slow enough to be directly observed via time-lapse optical microscopy [14–19]. Moreover, they are often much larger than the interaction range or the size of ions or ligands, which facilitates theoretical modeling and large-scale simulation of the crystallization pathways [14,20,21]. They have been thus viewed as excellent model systems for the study of a variety of crystallization-based phase transitions including nucleation, growth, melting, glass transitions, and solid–solid transitions [3].

The gap of understanding lies in crystals formed from nanoparticles, which have distinct shapes, complicated surface chemistry and comparable sizes with environmental factors, excluding simplification in

* Corresponding author at: Department of Materials Science and Engineering, University of Illinois, Urbana, IL 61801, United States.

E-mail address: qchen20@illinois.edu (Q. Chen).

modeling. In fact, it has been pointed out that their interactions are complicated and hard to model or simulate due to multiscale coupling and nonadditivity [22]. Extensive research has been performed on engineering nanoparticle superlattices due to their superior and tailorable properties. Their applications depend on structure, dimensionality, domain size, defects, polymorphism of the structure which is correlated with the formation pathways [1,2,23]. However, fundamental understanding of crystallization theories such as thermodynamics and the growth kinetics has been lacking to provide a unified conceptual framework for nanoparticles. It should be noted that the size between micron-sized colloids and atoms—both length scales better studied—exists a difference of 3 to 4 orders of magnitude, giving rise to their fundamental inconsistencies in phase transitions. For example, the crystals assembled from microspheres exhibit a relatively rough surface profiles in comparison with the atomic crystals at equilibrium, and the prevalent assembly mechanisms occur at atomic systems such as coalescence and oriented attachment have not been observed in micron-sized colloids [22,24–28]. This can be attributed to the short-range nature of interactions and slow dynamics of micro-sized colloids compared with atoms, both of which impart the colloidal particles more prone to kinetic traps and account for a more corrugated energy landscape [22,26–28]. Nanoparticles with their intermediate length scales can bridge this gap because nanoparticles are readily fabricated with more shapes and bonding geometries, showing relatively longer-ranged interactions and faster Brownian motions than micron-sized colloids [29]. In addition, the transition pathways of these crystals are expected to be more complicated than micron-sized colloids, owing to the increased importance of external fluctuations since the building blocks, solvent and ligand molecules exhibit comparable length scales [22,30–32].

Nevertheless, the crystallization of nanoparticles into superlattices is still mostly understood on a case-by-case basis. *In-situ* studies has been

limited due to the challenges of direct imaging at the single-nanoparticle resolution. Most *in-situ* characterizations of superlattice in the solution utilize small-angle X-ray scattering (SAXS), which provides structural information in reciprocal space [33–36]. Despite the minimal disturbance to the solution samples, SAXS is limited by its ensemble measurement, not capable of imaging detailed interaction events and capturing spatial heterogeneity, which is particularly pronounced at the onset of phase transitions, such as the formation of crystallite embryos, the initial appearance of symmetry switch during a solid–solid transition, and fusion of islands as well as annealing of defects. Transmission electron microscopy (TEM) provides nanometer and even atomic spatial resolution, but the challenge is also well-known; TEM is not traditionally compatible with nanoparticles in suspension as the samples need to be kept in high vacuum [37].

Thus liquid-phase TEM has emerged as a wonderful tool for studying nanoparticle superlattice formation by directly observing the dynamics of nanoparticles in solution, while also opening a new avenue for understanding materials science, such as catalysis and electrochemistry, etching and growth, and nucleation of atomic crystals [38–41]. In this mini review, we will focus on our group's and others' recent work studying the nucleation, and post-nucleation growth of nanoparticles into superlattices. We will discuss the similarities and differences of the observed nanoparticle superlattice formation process with the pioneering growth theories developed in atomic systems, as well as engineering opportunities to shape and achieve quality control (e.g., control of defects and surface morphologies) in superlattice formation from nanoparticles, for next-generation optical and mechanical metamaterials.

2. Adaptation of liquid-phase TEM for nanoparticle superlattice studies

There are three aspects of adaption of liquid-phase TEM for studying

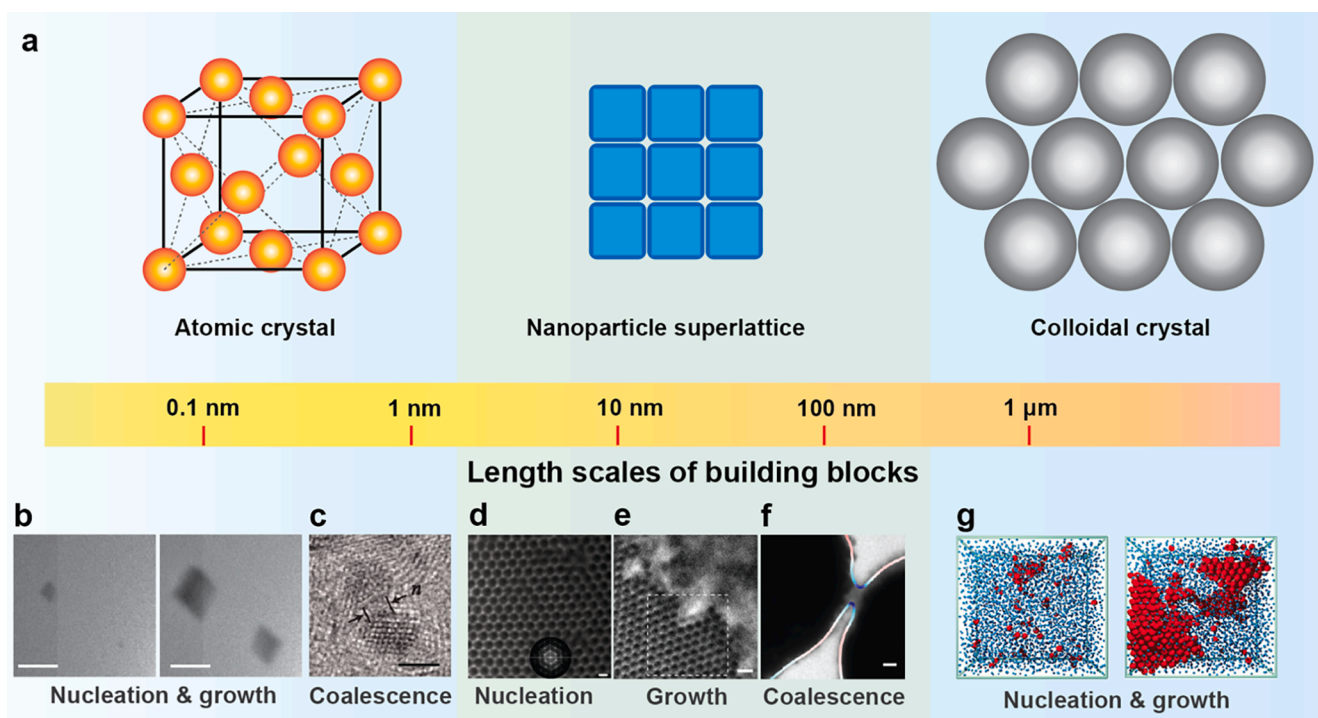


Fig. 1. Building blocks forming crystals at different length scales. (a) Schematic showing building blocks and the crystals they form into across the length scales over four orders of magnitude. (b and c). Examples of nucleation and growth (b), and coalescence (c) process of atomic crystals. (d–f) Examples of nucleation (d), growth (e), and coalescence (f) process of nanoparticle superlattice. (g) Examples of nucleation and growth in colloidal crystal. Scale bars: 500 nm in (b); 100 nm in (c) and (f); 200 nm in (d); 300 nm in (e). (b) Adapted with permission from Ref. [73]. Copyright 2014 American Association for the Advancement of Science. (c) Adapted with permission from Ref. [24]. Copyright 2012 American Association for the Advancement of Science. (d) Adapted with permission from Ref. [42]. Copyright 2020 Springer Nature. (e) Adapted with permission from Ref. [93]. Copyright 2020 Springer Nature. (f) Adapted with permission from Ref. [61]. Copyright 2019 American Chemical Society. (g) Reproduced with permission from Ref. [14]. Copyright 2001 American Association for the Advancement of Science.

nanoparticle superlattices, including controlling dose rate effects, minimizing and manipulating nanoparticle-substrate interaction, and single nanoparticle tracking which we detail as below.

To accommodate the high vacuum of TEM, we seal the nanoparticle suspension in a chamber using two SiN_x chips. Two methods can be used to trigger crystalline assemblies of nanoparticles while taking the TEM movies such that the onset of phase transition can be captured. One is to use liquid flow to introduce solvents of different properties (e.g., pH, ionic strength, polarity) during imaging, to change solvent-mediated nanoparticle interactions. The second is to utilize the beam effects, as radiolysis of water produces charged species (e.g., e^- , H^+ , OH^- , HO_2^- , O^- , O^{2-} , and O^{3-}), which increases the ionic strength in the imaging region and promotes screening of the electrostatic repulsions when the nanoparticles are charged (Fig. 2a) [42]. Other effects may also play a role in influencing the local ionic strength, such as a beam induced electric field owing to the emission of Auger and secondary electrons of the insulating SiN_x substrate [43–45]. In atomic level, this effect can even alter the Gibbs free energy of nucleation and random Brownian atomic diffusion, further having impact on the nucleation and growth process [43,46].

Both predictions based on reaction network of radiolysis [41] and our experimental work [47] show that the charged species have been shown to reach at a steady condition quickly upon (milliseconds of) illumination (Fig. 2b–d), providing a quantitative and stable control of nanoparticle interactions.

To quantify the effect of radiolysis species on nanoparticle interaction, we employed a one-dimensional (1D) superlattice assembled from gold triangular nanoprisms as an “ion” meter to monitor beam-induced ion generation, and correlated liquid-phase TEM with SAXS [47]. The superlattice has an equilibrium lattice constant of d spacing, the nearest neighboring prism-to-prism distance, responding selectively to the local ionic strength. We measured the one-to-one relation of d spacing versus dose rate under liquid-phase TEM and d spacing versus ionic strength using SAXS, to correlate the electron beam dose rate and ionic strength. As shown in the dose rate diagram (Fig. 2d) [47,48], at low electron dose rates ($<1 \text{ e}^- \text{ \AA}^{-2} \text{ s}^{-1}$), no structural change of the superlattice was observed under liquid-phase TEM. This is a regime that can be employed for imaging systems with low tolerance to radiolysis products, such as polymers and electrochemical process [37,49–51]. At intermediate

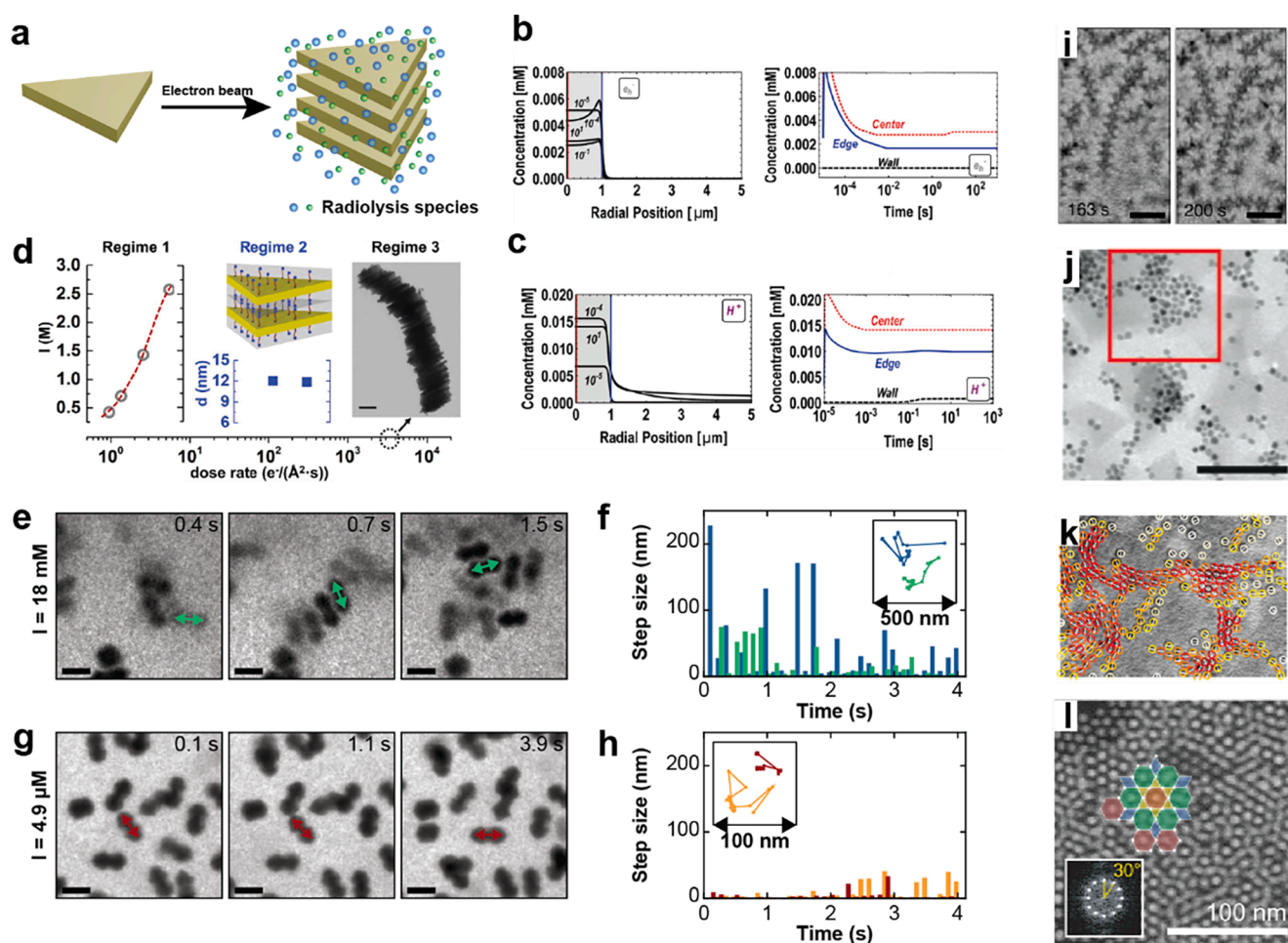


Fig. 2. Adaptation of liquid-phase TEM for nanoparticle superlattice studies. (a) Schematic showing the assembly due to the increased ionic strength under the illumination of electron beam. (b and c) Plot shows the heterogeneous model predictions for the spatial and temporal evolutions of e^- (b) and H^+ (c). (d) Chart diagram of the electron beam dose rate effect on the interaction and assembly of gold nanoprisms. (e–h) Time-lapse liquid-phase TEM images (e, g) of GNAs and step sizes (time interval: 0.12 s) and trajectories (inset) (f, h) of GNAs at (e, f) $I = 18 \text{ mM}$ and (g, h) $I = 4.9 \mu\text{M}$. The GNAs at higher ionic strength move more freely. (i–l) Liquid-phase TEM images of (i) 1D superlattice from CdSe/CdS octopods, (j) 2D hexagonal superlattice from Pt nanoparticles, (k) loosely hexagonal closed packed superlattice from magnetic Pt-Fe nanoparticles, and (l) 3D quasi-crystalline structures from oleylamine-coated Au nanoparticles. Scale bars: 50 nm in (d); 100 nm in (e), (g), (j) and (l); 200 nm in (i). (b and c) Reproduced with permission from Ref. [41]. Copyright 2014 American Chemical Society. (d) Reproduced with permission from Ref. [47]. Copyright 2016 American Chemical Society. (e–h) Reproduced with permission from Ref. [61]. Copyright 2020 American Chemical Society. (i) Reproduced with permission from Ref. [40]. Copyright 2016 Springer Nature. (j) Reproduced with permission from Ref. [62]. Copyright 2012 American Chemical Society. (k) Reproduced with permission from Ref. [63]. Copyright 2017 American Chemical Society. (l) Reproduced with permission from Ref. [64]. Copyright 2020 American Association for the Advancement of Science.

electron dose rates ($<5.5 \text{ e}^{-}\text{\AA}^{-2}\text{s}^{-1}$), the morphology of the nanoprisms maintains intact. The radiolysis species do not react with metal nanoparticles but change the ionic strength that screens the electrostatic interaction, as indicated by one-to-one relation of dose rate versus ionic strength. If the electron beam dose increases to $\sim 6\text{--}300 \text{ e}^{-}\text{\AA}^{-2}\text{s}^{-1}$, the superlattice contracted to a physical limit where the ligand layers of adjacent prisms were in physical contact. The intermediate electron dose rate regime offers us an experimental window, where the electron beam serves as a predictable and quantitative handle to alter the interactions of nanoscale entities and trigger the assembly *in situ*. At an even high dose rate (e.g., $3400 \text{ e}^{-}\text{\AA}^{-2}\text{s}^{-1}$), electron beam can decompose and/or strip off surface ligands on nanoparticles. Adjacent prisms came into physical contact, fusing into a single rod-shaped mass of gold. Shape transformation of inorganic nanoparticles has been prevalently investigated in this regime where the redox environment inside the chamber is altered, such as etching, nucleation, and growth [52–56].

The diffusional dynamics of nanoparticles determine how fast they approach, interact, and sample the free energy landscape of crystallization. Maintaining fast motion of nanoparticles under the liquid-phase TEM to anneal defects and diffuse out of a kinetic trap is thus a key experimental advancement which enables the crystallization of individual nanoparticles into superlattices. In liquid-phase TEM, it has been shown that diverse complications—strong particle–substrate attraction (e.g., van der Waals or electrostatic attraction) and confined liquid layers—can lead to sluggish nanoparticle motions [57–60]. For example, commercial SiN_x substrates can be positively charged as balanced by input and output currents upon beam illumination [59]. In our system of gold nanoarrows (GNAs), when dispersed in deionized water, the negatively charged GNAs can immediately stick on the substrate owing to electrostatic attraction, following Langmuir adsorption and “quenched” motions of nanoparticles (Fig. 2e and f). In the same system, increased ionic strength screens the electrostatic substrate–nanoparticle attraction, so that nanoparticles diffuse quickly and sample the free energy landscape efficiently, leading to the formation of degenerated lattices (Fig. 2g and h) [61].

With these optimized conditions, studying nanoparticle superlattice in liquid-phase TEM becomes an emerging field, wherein formation process of superlattices in different dimensions from 1D to 3D (Fig. 2i–l), using different nanoparticles (*i.e.*, shape and chemical composition) through various mechanisms, can be deciphered. The earliest report of the real-time nanoparticle superlattice formation on the SiN_x substrate can be dated back to the year of 2012 (Fig. 2j), in which Park and co-workers assemble Pt nanoparticles using capillary forces of the evaporating solvent front due to the electron beam irradiation and followed by relaxing to ordered superstructures through solvent fluctuations [62]. The superstructures can be further diversified by employing nanoparticles of more sophisticated shapes, for example CdSe/CdS octapods assembled to 1D interlocked superlattice in toluene, consistent with the observation *ex situ* [40] (Fig. 2i). Based on the statistical mechanics modelling of chain-length distribution, the authors reveal the underlying importance of dipolar and entropic forces in the assembly process. Serving as building blocks, the magnetic particles bring about additional anisotropy. In the case of Pt-Fe nanoparticles (Fig. 2k), the long-range magnetic interactions initially form highly aligned chain segments, followed by chain folding producing loosely packed hexagonal close-packed lattice to maximum short-ranged van der Waal interactions [63]. A series of 3D superlattices are realized by multiple-layer stacking of oleylamine-coated Au nanoparticles through fine tuning the substrate-particle interaction. Superlattice consisting of hexagonal honeycomb and quasi-crystalline structures are observed (Fig. 2l), based on the dielectric constant of the suspension solvent [64]. These examples suggest the power of the liquid-phase TEM in digging out the encoded information and underlying mechanisms that are otherwise inaccessible.

Lastly, the information on particles dynamics and interactions is embedded within TEM videos, which needs to be extracted using particle tracking algorithms. The size of liquid-phase TEM videos ever

grows owing to the development of fast detectors capable of capturing hundreds to thousands of frames per second [65]. Methods that could automatically process and analyze the huge data files consisting of temporal stacks of spatial images are highly required by addressing the following analysis challenges unique to liquid-phase TEM data. First, liquid layer and window of liquid chamber reduce the TEM contrast between the nanoparticles and background [24,54,62,66]. Second, shot noise of a Poisson nature increases with lowered dose rates, which together with the low image contrast makes liquid-phase TEM videos with a low signal-to-noise ratio (SNR) [67]. For these low SNR TEM videos, it is hard for conventional image analysis algorithms based on single intensity threshold to precisely identify features from the background without frequent human supervision.

To tackle the challenges, the third development we pushed is to employ machine learning to analyze liquid-phase TEM videos. Machine learning based imaging analysis has shown great success in various fields, such as biomedical image diagnosis [68], self-driving automobile [69], and facial recognition [70]. We chose the U-Net convolutional neural network (NN) (Fig. 3a) [71], which was presented by Olaf Ronneberger and co-workers [72]. In doing so, we demonstrated automated processing of liquid-phase TEM movies to extract three types of nanoscale dynamics, including a interparticle interaction landscape of highly anisotropic nanoprisms, curvature-dependent and staged etching profiles of gold nanorods, and structural motifs in thermodynamic ground state and kinetic laws of chain formation of nanocubes. These examples cover representative scenarios and challenges in quantifying and analyzing the experimental data under liquid-phase TEM, and, for a video consisting of thousands of frames, it only takes <1 min for a trained NN model to finish segmentation (Fig. 3b–d), both of which facilitate the understanding of physical parameters during crystallization from nanoparticles in a quantitative manner.

3. Nucleation of nanoparticle superlattices at the nanoscale

Nucleation is the initial and crucial step in determining physical properties of crystals [73]. Due to the stochastic nature of nucleation and growth, the kinetic pathways of crystallization are difficult to be depicted at theoretical level. For example, the kinetics of such first-order phase transitions is often complicated and still lacks unified theory at the fundamental level [74]. For atomic systems, crystal embryo usually forms from the liquid phase *via* nucleation. Small nuclei tend to grow only when they overcome a free-energy barrier, namely exceeding a critical size [75]. The formation of the critical nucleus at the initial stage is difficult to observe and characterize owing to the small temporal and spatial scales. Previous *in-situ* paradigms of crystallization thus concentrated on ensemble characterization of nucleation rates and kinetics (e.g., in protein crystallization) and direct imaging of micron-sized colloids as model systems which are convenient to observe under optical microscopy [6,14]. Deviations from the classical nucleation theory have been frequently observed as non-classical nucleation pathways for those systems [1,75]. As shown in Fig. 4a–c, depending on the energy landscapes that vary in shape and energy magnitudes corresponding to their thermodynamic origins, three crystallization pathways can be identified, including monomer-by-monomer nucleation-and-growth pathway predicted by classical nucleation theories (Fig. 4a), aggregation of metastable particles, consisting of amorphous, liquid, and poorly crystalline particles, and/or oriented attachment of metastable nanocrystals (Fig. 4b), crystallization of nanoparticles *via* a two-step pathway involving the formation of a metastable intermediate phase, such as a liquid or solid polymorph (Fig. 4c). For nanoparticles, liquid-phase TEM has been utilized to monitor the dynamics and interactions of nanoparticles of various shapes *in situ* for a decade, wherein particles of various structures can self-assemble to 1D chain and 2D patterns [40,59,63,76–79]. Observations of formation of superlattice at solid–liquid interfaces or through controlled solvent [62,80] have also been made, showcasing its power in resolving practically manufactured

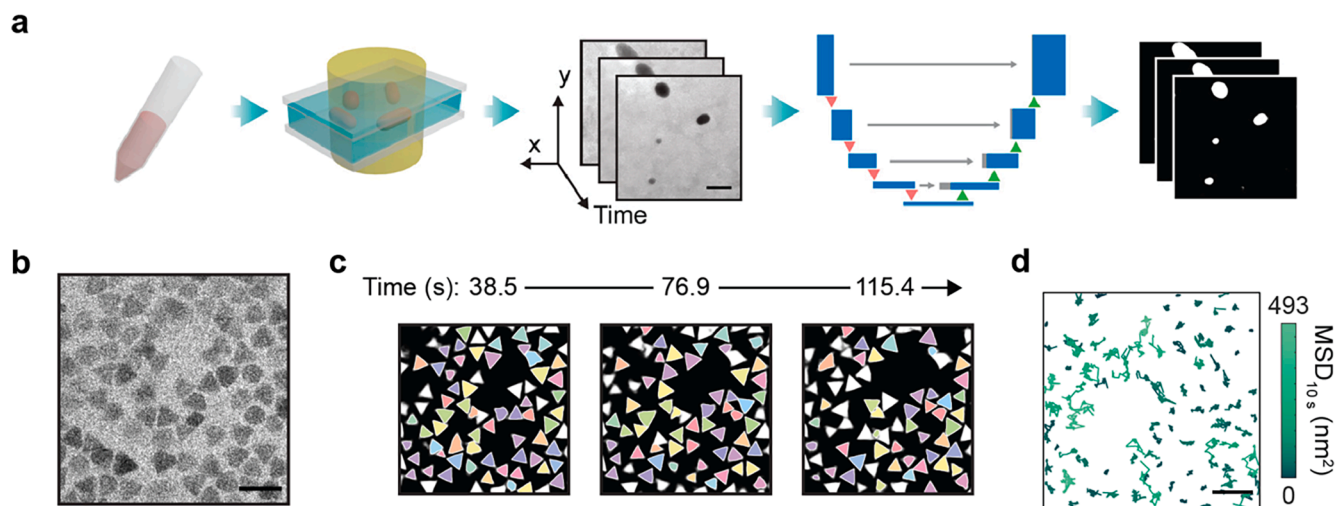


Fig. 3. Information of liquid-phase TEM extraction with the aid of machine learning. (a) Workflow of U-Net-based liquid-phase TEM video segmentation. (b) A snapshot of gold nanoprisms under liquid-phase TEM. (c) Tracked nanoprisms of a time-lapse liquid-phase TEM using U-Net prediction. (d) Tracking trajectory of nanoprisms with color label of mean-squared displacement (MSD) at a 10 s time interval. Scale bars: 200 nm in (a) and (e). (a–d) Reproduced with permission from Ref. [71]. Copyright 2020 American Chemical Society.

nanoparticle superlattices. Recent reviews of the dynamics, interactions, and pre-assembled superlattice of nanoparticles are available in the literatures [81,82]; in this mini review we focus on the *in-situ* observation of formation and growth process of nanoparticle superlattices.

Built on the three advancements discussed in Section 1, we utilized liquid-phase TEM to achieve real-space *in-situ* observation of non-classical nucleation during the formation of superlattices. In this work of gold triangular nanoprisms of high particle concentration, complex hierarchical lattices [42] are formed. Individual nanoprisms recognize shape anisotropy and initially stack into misaligned columns along the *z* direction, due to the balance between van der Waals attraction and electrostatic repulsion. Each column then serves as a secondary building block in the *x*-*y* plane and move freely, which we follow using tracking algorithms, to form into a hexagonal columnar lattice. Liquid-phase TEM records the crystallization process, and we monitored it by measuring local bond-orientational order and local density. The initially well-dispersed columns (gas phase) condense into a metastable “liquid” cluster with a relatively long lifetime, within which the ordered “solid” phase nucleates and propagates (Fig. 4d and e). The radially isotropic interactions between columns promote their hexagonal packing and form the large-scale crystal structure (Fig. 4f).

The liquid-like phase is a metastable intermediate that is characteristic of a two-step crystallization process. This two-step process agrees with a phenomenological two-barrier free energy, where the intermediate liquid state acts as a ‘wetting’ layer that lowers the interfacial tension, so that ordering happens within. This can be attributed to the fact that the interfacial energy dominates when a nucleus is small. Liquid-like intermediate tends to exist because the liquid–gas interfacial energy is lower than the crystal–gas interfacial energy [83]. Such pathway has been observed in micron-sized particles and dilute state in proteins, featuring liquid to denser liquid cluster to crystal, and liquid to ordered low-density cluster to crystal [6,20,84]; our observation of nonclassical nucleation extended the observation to colloidal nanoparticles.

Multistep crystallization, involving gas state, cluster state, polycrystalline, and single crystalline solid states, is realized in nonaqueous solutions under liquid-phase TEM, as indicated by the time-lapse liquid-phase TEM images overlaid with bond order parameters (Fig. 4g) [85]. The building blocks are the gold nanoparticles grafted with thiol-terminated polystyrene, which are well-dispersed in nonpolar solvent, e.g., octane (dielectric constant $\epsilon = 1.95$), but exhibit severe random aggregation in solvent with relatively high dielectric constant, in this

case butanol ($\epsilon = 17.84$). The diffusivity of nanoparticles also shows the positive correlation with the dose rate under low dose ($<10.0 \text{ e}^{-\text{\AA}^{-2}\text{s}^{-1}}$), eventually reaching up to $3.1 \times 10^3 \text{ nm}^2\text{s}^{-1}$. The crystalline two-dimensional superlattice arises, when a mixture of octane/butanol ($v/v = 1:1$) is in use, in which the moderately attractive interaction favors the crystallization rather than irregular aggregation of those highly dynamic particles. Initially, the most particles are monomers, assembling into dimers, trimers, and oligomers, and then form small clusters. These small clusters are not stable, reconfiguring frequently and becoming large clusters. The large clusters coalesce to a whole but poorly crystalline domain, followed by evolving into large single-crystalline domain. 6-fold bond orientational correlation function $g_6(r, t)$ shows a time dependence of $R_6 \sim (t - t_0)^{0.33}$, indicating anomalous grain-growth behaviors due to stress-assisted grain growth, grain rotation, and microstructures of grain boundaries. This work enriches the degree of control for studying crystallization process and phase transition kinetics.

The capability of imaging the nanoparticles at the onset of a phase transition at the single particle level also offers systematic study of phase transitions other than crystallization, such as melting, sublimating, crystal–crystal transitions, and glass transition for nanoparticles as building blocks.

4. Morphology development of superlattices during post-nucleation growth

Surface morphology and shape of crystalline nanostructures play a central role in determining their physical properties and applications, which are developed during the crystal growth process after nucleation (Fig. 5a) [86–90]. The theory involved has studied for atomic systems over the past few decades. For example, the Wulff construction rule is prevalently utilized to predict the shape of a crystal in its thermodynamic ground state by considering the surface energies of different facets of a crystal [91,92]. Such construction rule can be further extended to Winterbottom and Summertop constructions when the growth of the crystals is confined on a substrate [10]. To predict surface morphology of crystals, or the smoothness of a crystalline layer, a variety of models on kinetic growth modes such as the Stranski–Krastanov, Frank–van der Merwe, and Volmer–Weber models have been developed, weighing the balance of factors such as surface energy, binding energy, and diffusional dynamics [8,9].

To understand the morphology development of nanoparticle

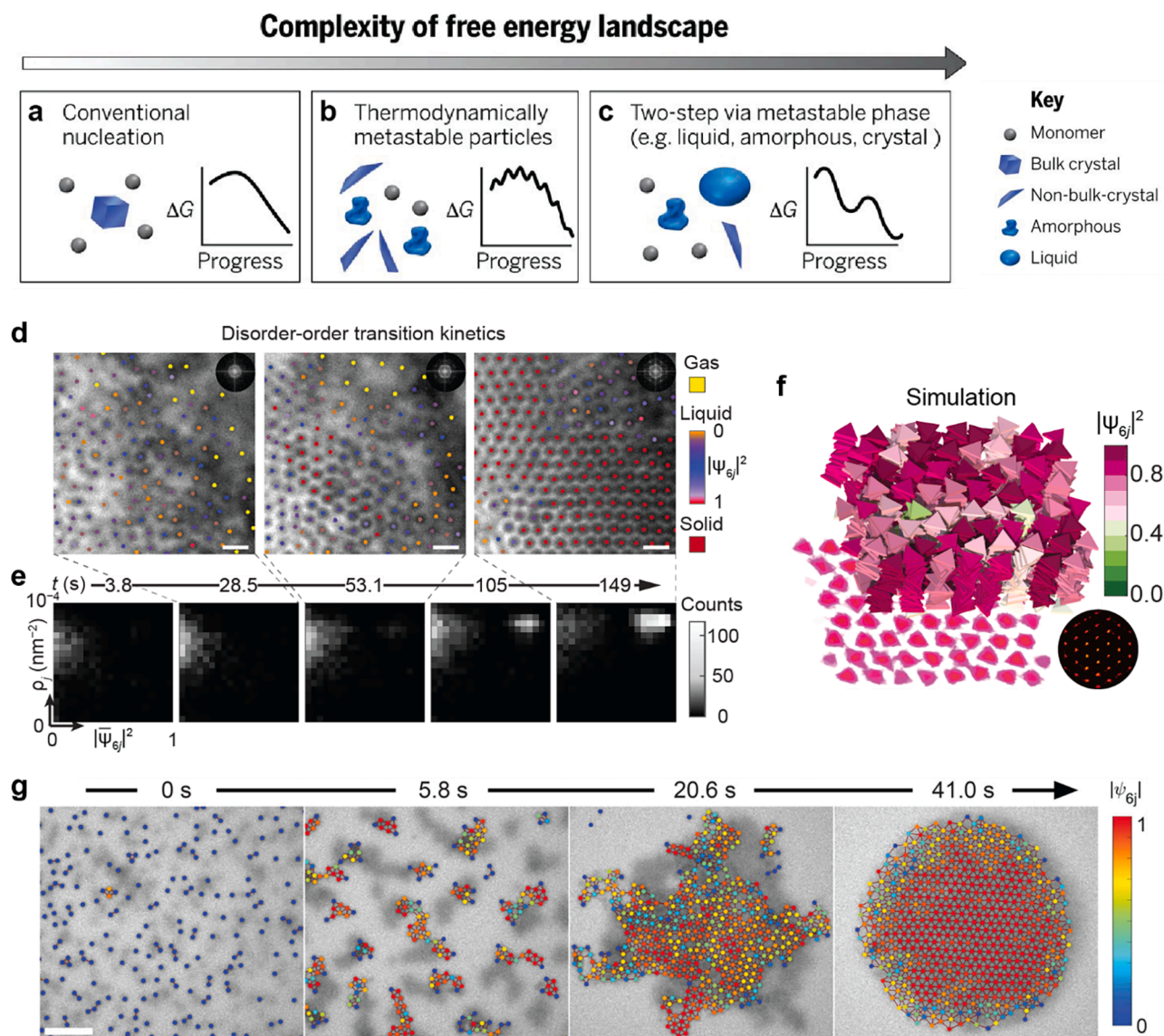


Fig. 4. Nucleation of superlattice. (a–c) Schematic showing the energy landscape of various scenario of nucleation, including (a) classical monomer-by-monomer addition, (b) aggregation of metastable particles, such as liquid, amorphous, or poorly crystalline particles, or of oriented (and nearly oriented) attachment of metastable nanocrystals, and (c) crystallization via an intermediate state, such as a liquid or solid polymorph. (d) Time-lapse liquid-phase TEM images show the real-time crystallization process at high particle concentration, with ‘gas’ columns, ‘liquid’ columns and ‘solid’ columns colored as indicated in color bar. (e) Corresponding order-density histograms. (f) Monte Carlo (MC) simulations confirm that the hexagonal lattice is the thermodynamically stable state of the misaligned columns. (g) Time-lapse liquid-phase TEM images of the multistep crystallization of nanoparticles in a mixed organic solvent overlaid with 6-fold bond-orientational order parameters. Scale bars: 200 nm in (d); 500 nm in (g). (a–c) Adapted with permission from Ref. [1]. Copyright 2015 American Association for the Advancement of Science. (d–f) Reproduced with permission from Ref. [42]. Copyright 2019 Springer Nature. (g) Reproduced with permission from Ref. [85]. Copyright 2022 American Chemical Society.

superlattices, we used liquid-phase TEM to observe the kinetics of how nanoparticles attach one by one onto the growing crystal surface. Such experimental data are inaccessible from either *ex-situ* real-space measurements based on previous protocols, namely electron microscopy images of discrete stages of the growth process in dried samples, or from *in-situ* reciprocal space characterizations like SAXS. By combining capillary wave theory (CWT) and direct imaging of a fluctuating surface of a growing superlattice, we successfully extracted and analyzed the surface energies of different facets [93].

As shown in Fig. 5b, the lattice orientation of the superlattice stays unchanged during the growth, indicating that the system is in a stable state without accumulating beam effects and changing interaction environment. In the meantime, due to the anisotropic interfacial stiffness, its surface orientation undergoes a shift that separate the

superlattice growth process into two stages, where the surface orientation θ exhibits a 19 % increase, from $\theta = (36 \pm 6)^\circ$ for the first stage (~ 100 s) to $\theta = (49 \pm 5)^\circ$ for the second stage (~ 50 s). The surface orientation changes from a high index (340) facet to a low index (210) facet, suggesting that exposed facets (and the growth direction) of the superlattice shifts to lower surface energy state, which is thermodynamically favored (Fig. 5b). The observed orientation convergence is also consistent with the notations in atomic crystals that facets of lower Miller indexes tend to have a lower surface energy and be more favored to be exposed at the crystal surface [91]. Consequently, the surface roughness of the superlattice lattice also becomes smaller (Fig. 5c), consistent with flat-faceted polygonal shapes of nanoparticle superlattices at equilibrium formed *ex situ* [92,94–96].

The direct observation of the surface profiles of the superlattice al-

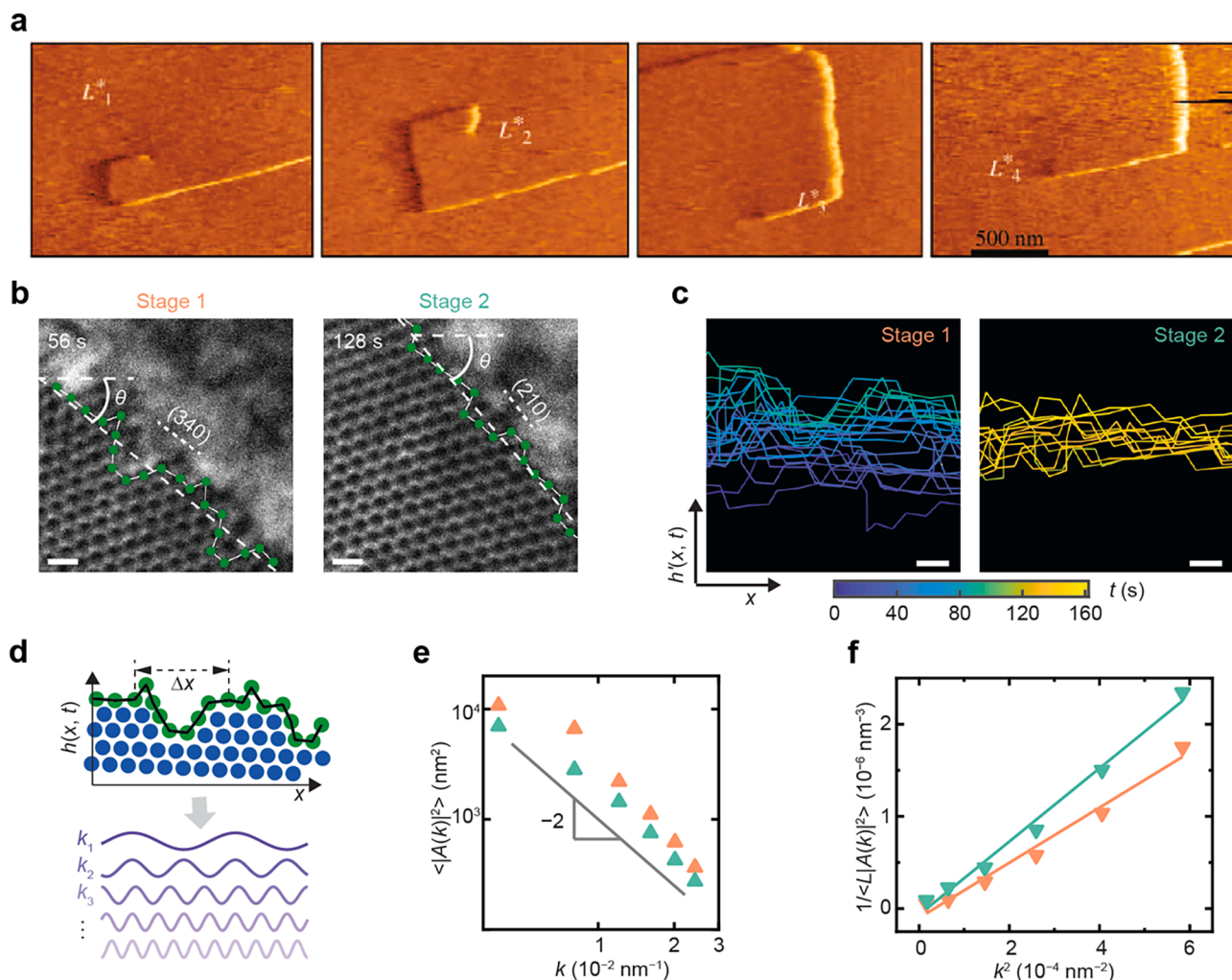


Fig. 5. Morphology determination of nanoparticle superlattice during post-nucleation growth. (a) Time-lapse atomic force microscopy images showing development of a polygonized spiral step. (b) Representative liquid-phase TEM images for first stage and second stage highlighting the surface orientation shift. (c) Time-dependent surface profiles of the developing superlattice. The elapsed time is coded by the color (4 s interval). (d) Schematic illustrating the Fourier decomposition of the height function $h(x, t)$ into a series superimposed waves having different wave vectors. (e) Dependence of $\langle |A(k)|^2 \rangle$ as a function of k on a log–log scale plot for both stage 1 (salmon) and stage 2 (aquamarine). (f) Linear fitting of $1/\langle L|A(k)|^2 \rangle$ as a function of k^2 overlaid with the corresponding linear fitting lines for the two stages. Scale bars: 500 nm in (a); 200 nm in (b) and (c). (a) Reproduced with permission from Ref. [90]. Copyright 2004 Springer Nature. (b–f) Reproduced with permission from Ref. [93]. Copyright 2020 Springer Nature.

allows us to validate and apply CWT to quantitatively measure anisotropic interfacial stiffness and interfacial mobility (Fig. 5d). CWT describes how a surface fluctuates due to a balance of thermal fluctuation (roughening) and surface energy (smoothing) and has been applied to micron-sized colloids and atoms [97–102]. Specifically, the surface profiles of the crystal surfaces can be decomposed into a series of Fourier modes. The correlation between time-averaged Fourier coefficient $\langle |A(k)|^2 \rangle$ and wave vector k follows a power law of -2 as expected from CWT (Fig. 5e). Moreover, the parameter of interfacial mobility relating the interfacial normal velocity to the driving force also suggests that no bulk driving forces other than thermal fluctuation exists in this system. The interfacial stiffness $\tilde{\gamma}$ at these two growth stages was calculated based on CWT, revealing the dependence on surface orientation. As shown in Fig. 5f, the linear fitting of $1/\langle L|A(k)|^2 \rangle$ as a function of k^2 enables us to measure the interfacial stiffness $\tilde{\gamma}/k_B T$ as the slope. The interfacial stiffness values of both stages were calculated to be on the order of 10^{-14} J m $^{-1}$, agreeing well with interface stiffness scaling as $\sim k_B T/l_c$, where l_c is the size of the building block, which was measured as 120 nm in this system. The interfacial stiffness exhibits 32 % increases, from $(1.23 \pm 0.09) \times 10^{14}$ J m $^{-1}$ for the first stage to $(1.63 \pm 0.08) \times 10^{14}$ J m $^{-1}$ for the second stage, accounting for the lower

surface roughness, owing to the fact that the surface orientation with higher interfacial stiffness indicates that of lower surface energy. Such trend benefits the growing superlattice to effectively lowers their surface energy, which is consistent with the Wulff construction rule exhibiting flatter surface with lower surface energy facets for an equilibrium crystal shape [10,91,92].

5. Coalescence of nanoparticle assemblies

At the atomic level, apart from growth *via* monomer attachment, the coalescence of nanoparticles is another important pathway for nanocrystal growth, as demonstrated in liquid-phase TEM studies of Pt nanocrystals' coalescence (Fig. 6a) [24,55]. The driving force can be ascribed to the generic instability of nanoparticles due to their large surface-to-volume ratio, so that small particles reduce the surface energy by collision and coalescence to form a big particle with smaller relative surface exposed [103]. Generally, coalescence happens through one or several of the four types of mass transport modes, which are surface diffusion, volume diffusion, hydrodynamic flow, and evaporation–condensation [104]. For atomic crystals smaller than 1 μ m and a temperature below the bulk melting point, surface diffusion is

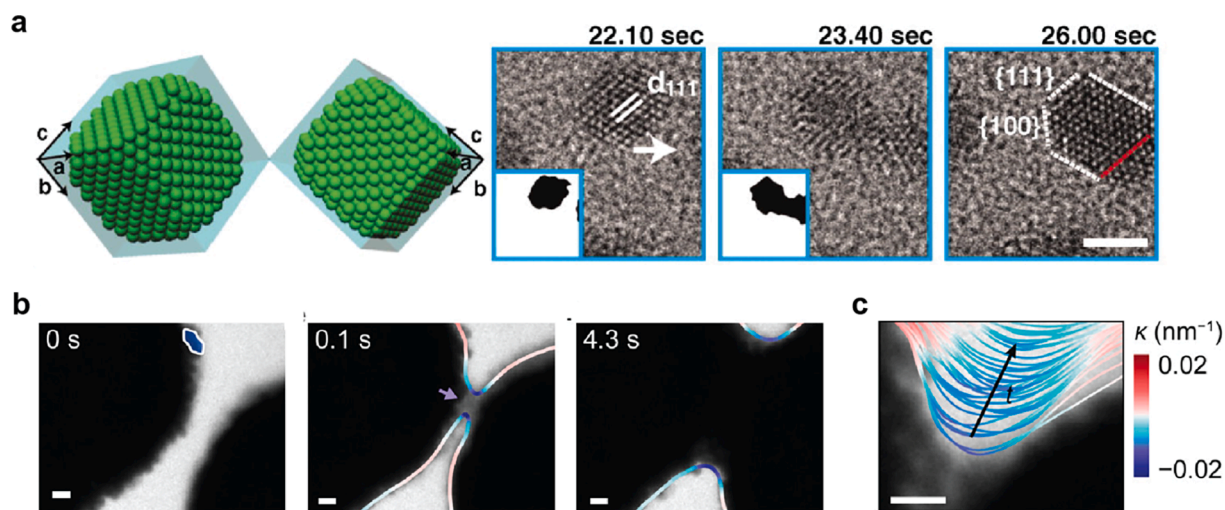


Fig. 6. Coalescence of nanoparticle superlattice. (a) Cartoon and time-lapse liquid-phase TEM images showing the coalescence process of two Pt nanocrystals. (b) Time-lapse liquid-phase TEM images showing the coalescence of two large clusters. (c) Time-lapse contours of the developing contact neck overlaid with the TEM image (0.12 s time interval). Scale bars: 2 nm in (a); 100 nm in (b) and (c). (a) Adapted with permission from Ref. [24]. Copyright 2012 American Association for the Advancement of Science. (b and c) Reproduced with permission from Ref. [61]. Copyright 2020 American Chemical Society.

considered as the dominant mass transport route [105]. To specify the possible contributions from multiple mechanisms, a power law $d_{neck} \sim t^a$ is expected, where d_{neck} is the width of the contact neck of the particle after coalescence, t is time, and a is a constant depending on the diffusion type. The constant a of surface diffusion is about 0.16 as predicted by the classical continuum theory [104–106]. Deviation of a value on the high side arises, especially at the early stage of coalescence, when the highly curved neck region generated after the coalescence, which offers high coordinate sites for material diffusion and redistribution [103]. Such power law dependence has been verified in the coalescence of atomic crystals studied using liquid-phase TEM [55,103]. Coalescence has not been observed in crystallization from micron-sized colloids, possibly due to the absence of efficient surface, edge, and volume diffusions. We demonstrate that faster diffusion of nanoparticles makes it possible for superlattices to realize the coalescence growth [61].

In our recent study using negatively-charged gold GNAs [61], at ionic strength $I = 6.4$ mM, local concaveness of GNAs favors them to assemble into the dynamic “zipper” motif, as explained by the combined interparticle van der Waals attraction and electrostatic repulsion corresponding to various pairwise configurations. At a higher ionic strength $I = 120$ mM, the electrostatic interactions are further screened and the GNAs form larger assemblies which display coalescence growth analogous to that in atomic crystallization. At low GNA concentration, the clusters assembled from GNAs are small (<30 GNAs), diffusing and rearranging quickly as a whole after coalescence. While, as a comparison, when the GNA concentration is high, the clusters are large (>100 GNAs) and diffuse slower, displaying the formation of a neck as two clusters of GNAs come into physical contact (Fig. 6b). The high-curvature regions of the coalescing neck decrease while regions of low curvature remain during the coalescence (Fig. 6c). This tendency agrees with that minimization of the free energy by reducing surface area drives the coalescence [107].

Importantly, the interapex distance measured as the neck width d_{neck} over time t shows a power law of $d_{neck} \sim t^{0.24}$, indicating surface diffusion mechanism predicted by classical continuum theory in atomic systems ($d_{neck} \sim t^{0.16}$) among the mass transport paths during coalescence. The surface energy gain for coalescence was calculated as $3.2k_B T$ following CWT, which is sufficient for the occurrence of coalescence.

6. Conclusion and outlook

The use of liquid-phase TEM to study the crystallization of

nanoparticle superlattices can bridge the length scale gap in crystal nucleation and growth. Built upon existing studies on model gold nanoparticles, four future directions can be further developed. First, nanoparticles can be synthesized with diverse shapes, sizes, and composition thanks to chemists’ decades of efforts [23]. Combined with direct imaging of particle dynamics and statistical-mechanics-based framework, this large toolkit of nanoparticles makes it possible to provide insight into how particles’ shape and interaction influence the nucleation and growth kinetics, and ultimately the crystal’s properties such as crystallinity, phase, shape to facilitate superlattice engineering. Second, as aforementioned, the dose rate changes the chemical environment of suspension media during assembly, further influencing interparticle interactions and diffusivity on the substrate. To minimize the beam effect, even lower dose can be applied in company with feasible detectors; meanwhile, scavengers and solvents with high resistance to radiation damage also reduce radical production [108], both of which are favorable to stable superlattice. Besides, the beam radiation also triggers the chemical reactions of ligands that can potentially change the surface properties for the *in-situ* reconfiguration [109]. Third, the current *in-situ* images are obtained from “top view”, which is not capable of resolving three-dimensional (3D) structures or inter-layer interactions. Future advancements on liquid-phase TEM such as tomography and scanning confocal transmission electron microscopy may realize three-dimensional imaging comparable to the micron-sized particles observed by confocal optical microscopy [14], revealing comprehensive phase transition pathways. Finally, active matter, which converts external energy input to bypass the entropy bottleneck and stays out-of-equilibrium, has become a new research paradigm in micron-sized particles, developing self-organized structures that are otherwise inaccessible at equilibrium and mimicking those of living organisms [110,111]. Analogously, beyond the quasi-equilibrium system we focus on here, more studies can emerge to use our protocol to investigate the systems that are active, with the aid of external stimuli.

Declaration of Competing Interest

The authors declare that they have no known competing financial interests or personal relationships that could have appeared to influence the work reported in this paper.

Data availability

For this review paper, request for the original data should be addressed to the authors of the papers accordingly.

Acknowledgement

The authors acknowledge support from U.S. Department of Energy, Office of Science, Office of Basic Energy Sciences, Division of Materials Science and Engineering, under award number DE-SC0020723.

References

- [1] J.J. De Yoreo, P.U. Gilbert, N.A. Sommerdijk, R.L. Penn, S. Whitelam, D. Joester, H. Zhang, J.D. Rimer, A. Navrotsky, J.F. Banfield, A.F. Wallace, F.M. Michel, F.C. Meldrum, H. Colfen, P.M. Dove, CRYSTAL GROWTH. Crystallization by particle attachment in synthetic, biogenic, and geologic environments, *Science* 349 (2015) aaa6760.
- [2] N.D. Loh, S. Sen, M. Bosman, S.F. Tan, J. Zhong, C.A. Nijhuis, P. Král, P. Matsudaira, U. Mirsaidov, Multistep nucleation of nanocrystals in aqueous solution, *Nat. Chem.* 9 (2017) 77–82.
- [3] B. Li, D. Zhou, Y. Han, Assembly and phase transitions of colloidal crystals, *Nat. Rev. Mater.* 1 (2016).
- [4] J.H. Choi, H. Wang, S.J. Oh, T. Paik, P. Sung, J. Sung, X. Ye, T. Zhao, B.T. Diroll, C.B. Murray, C.R. Kagan, Exploiting the colloidal nanocrystal library to construct electronic devices, *Science* 352 (2016) 205–208.
- [5] K. Henzler, E.O. Fetisov, M. Galib, M.D. Baer, B.A. Legg, C. Borca, J.M. Xto, S. Pin, J.L. Fulton, G.K. Schenter, Supersaturated calcium carbonate solutions are classical, *Sci. Adv.* 4 (2018) eaa06283.
- [6] P.R.T. Wolde, D. Frenkel, Enhancement of protein crystal nucleation by critical density fluctuations, *Science* 277 (1997) 1975–1978.
- [7] É. Ducrot, M. He, G.-R. Yi, D.J. Pine, Colloidal alloys with preassembled clusters and spheres, *Nat. Mater.* 16 (2017) 652–657.
- [8] J. Prieto, I. Markov, Stranski-Krastanov mechanism of growth and the effect of misfit sign on quantum dots nucleation, *Surf. Sci.* 664 (2017) 172–184.
- [9] H. Heo, J.H. Sung, J.H. Ahn, F. Ghahari, T. Taniguchi, K. Watanabe, P. Kim, M. H. Jo, Frank–van der Merwe Growth versus Volmer–Weber Growth in Successive Stacking of a Few-Layer Bi₂Te₃/Sb₂Te₃ by van der Waals Heteroepitaxy: the critical roles of finite lattice-mismatch with seed substrates, *Adv. Electron. Mater.* 3 (2017) 1600375.
- [10] L. Marks, L. Peng, Nanoparticle shape, thermodynamics and kinetics, *J. Phys.: Condens. Matter* 28 (2016) 053001.
- [11] A.A. Chernov, Protein crystals and their growth, *J. Struct. Biol.* 142 (2003) 3–21.
- [12] P.G. Vekilov, A.A. Chernov, The physics of protein crystallization, *Solid State Phys.*, Elsevier 2003, pp. 1–147.
- [13] A. Chernov, Protein versus conventional crystals: creation of defects, *J. Cryst. Growth* 174 (1997) 354–361.
- [14] U. Gasser, E.R. Weeks, A. Schofield, P.N. Pusey, D.A. Weitz, Real-space imaging of nucleation and growth in colloidal crystallization, *Science* 292 (2001) 258–262.
- [15] T. Palberg, Crystallization kinetics of colloidal model suspensions: recent achievements and new perspectives, *J. Phys.: Condens. Matter* 26 (2014) 333101.
- [16] Q. Chen, J.K. Whitmer, S. Jiang, S.C. Bae, E. Luijten, S. Granick, Supracolloidal reaction kinetics of Janus spheres, *Science* 331 (2011) 199–202.
- [17] Q. Chen, S.C. Bae, S. Granick, Directed self-assembly of a colloidal kagome lattice, *Nature* 469 (2011) 381–384.
- [18] Y. Wang, Y. Wang, D.R. Breed, V.N. Manoharan, L. Feng, A.D. Hollingsworth, M. Weck, D.J. Pine, Colloids with valence and specific directional bonding, *Nature* 491 (2012) 51–55.
- [19] M. He, J.P. Gales, E. Ducrot, Z. Gong, G.R. Yi, S. Sacanna, D.J. Pine, Colloidal diamond, *Nature* 585 (2020) 524–529.
- [20] P. Tan, N. Xu, L. Xu, Visualizing kinetic pathways of homogeneous nucleation in colloidal crystallization, *Nat. Phys.* 10 (2014) 73–79.
- [21] S.C. Glotzer, M.J. Solomon, Anisotropy of building blocks and their assembly into complex structures, *Nat. Mater.* 6 (2007) 557–562.
- [22] C.A. Silvera Batista, R.G. Larson, N.A. Kotov, Nonadditivity of nanoparticle interactions, *Science* 350 (2015) 1242477.
- [23] M.A. Boles, M. Engel, D.V. Talapin, Self-assembly of colloidal nanocrystals: from intricate structures to functional materials, *Chem. Rev.* 116 (2016) 11220–11289.
- [24] J.M. Yuk, J. Park, P. Ercius, K. Kim, D.J. Hellebusch, M.F. Crommie, J.Y. Lee, A. Zettl, A.P. Alivisatos, High-resolution EM of colloidal nanocrystal growth using graphene liquid cells, *Science* 336 (2012) 61–64.
- [25] X. Zhang, Y. He, M.L. Sushko, J. Liu, L. Luo, J.J. De Yoreo, S.X. Mao, C. Wang, K. M. Rosso, Direction-specific van der Waals attraction between rutile TiO₂ nanocrystals, *Science* 356 (2017) 434–437.
- [26] R. Ganapathy, M.R. Buckley, S.J. Gerbode, I. Cohen, Direct measurements of island growth and step-edge barriers in colloidal epitaxy, *Science* 327 (2010) 445–448.
- [27] N. Kleppmann, F. Schreiber, S. Klapp, Limits of size scalability of diffusion and growth: Atoms versus molecules versus colloids, *Phys. Rev. E* 95 (2017) 020801.
- [28] R. Xie, X.-Y. Liu, Controllable epitaxial crystallization and reversible oriented patterning of two-dimensional colloidal crystals, *J. Am. Chem. Soc.* 131 (2009) 4976–4982.
- [29] Y. Han, Seeing crystal formation one particle at a time, *Nat. Mater.* 19 (2020) 377–378.
- [30] X. Ye, J. Chen, M. Eric Irrgang, M. Engel, A. Dong, S.C. Glotzer, C.B. Murray, Quasicrystalline nanocrystal superlattice with partial matching rules, *Nat. Mater.* 16 (2017) 214–219.
- [31] Y. Xia, T.D. Nguyen, M. Yang, B. Lee, A. Santos, P. Podsiadlo, Z. Tang, S. C. Glotzer, N.A. Kotov, Self-assembly of self-limiting monodisperse supraparticles from polydisperse nanoparticles, *Nat. Nanotechnol.* 6 (2011) 580–587.
- [32] H. Lin, S. Lee, L. Sun, M. Spellings, M. Engel, S.C. Glotzer, C.A. Mirkin, Clathrate colloidal crystals, *Science* 355 (2017) 931–935.
- [33] Y. Zhang, S. Pal, B. Srinivasan, T. Vo, S. Kumar, O. Gang, Selective transformations between nanoparticle superlattices via the reprogramming of DNA-mediated interactions, *Nat. Mater.* 14 (2015) 840–847.
- [34] Y. Zhao, K. Thorkelsson, A.J. Mastroianni, T. Schilling, J.M. Luther, B. J. Rancatore, K. Matsunaga, H. Jinnai, Y. Wu, D. Poulsen, Small-molecule-directed nanoparticle assembly towards stimuli-responsive nanocomposites, *Nat. Mater.* 8 (2009) 979–985.
- [35] Y. Kim, R.J. Macfarlane, M.R. Jones, C.A. Mirkin, Transmutable nanoparticles with reconfigurable surface ligands, *Science* 351 (2016) 579–582.
- [36] F. Lu, K.G. Yager, Y. Zhang, H. Xin, O. Gang, Superlattices assembled through shape-induced directional binding, *Nat. Commun.* 6 (2015) 1–10.
- [37] F.M. Ross, Opportunities and challenges in liquid cell electron microscopy, *Science* 350 (2015) aaa9886.
- [38] J. Park, H. Elmlund, P. Ercius, J.M. Yuk, D.T. Limmer, Q. Chen, K. Kim, S.H. Han, D.A. Weitz, A. Zettl, 3D structure of individual nanocrystals in solution by electron microscopy, *Science* 349 (2015) 290–295.
- [39] H.-G. Liao, L. Cui, S. Whitelam, H. Zheng, Real-time imaging of Pt₃Fe nanorod growth in solution, *Science* 336 (2012) 1011–1014.
- [40] E. Sutter, P. Sutter, A.V. Tkachenko, R. Krahn, J. De Graaf, M. Arciniegas, L. Manna, In situ microscopy of the self-assembly of branched nanocrystals in solution, *Nat. Commun.* 7 (2016) 1–7.
- [41] N.M. Schneider, M.M. Norton, B.J. Mendel, J.M. Grogan, F.M. Ross, H.H. Bau, Electron–water interactions and implications for liquid cell electron microscopy, *J. Phys. Chem. C* 118 (2014) 22373–22382.
- [42] Z. Ou, Z. Wang, B. Luo, E. Luijten, Q. Chen, Kinetic pathways of crystallization at the nanoscale, *Nat. Mater.* 19 (2020) 450–455.
- [43] N. Jiang, Note on in situ (scanning) transmission electron microscopy study of liquid samples, *Ultramicroscopy* 179 (2017) 81–83.
- [44] N. Jiang, Damage mechanisms in electron microscopy of insulating materials, *J. Phys. D: Appl. Phys.* 46 (2013) 305502.
- [45] T. Gupta, N.M. Schneider, J.H. Park, D. Steingart, F.M. Ross, Spatially dependent dose rate in liquid cell transmission electron microscopy, *Nanoscale* 10 (2018) 7702–7710.
- [46] D. Kashchiev, Nucleation in external electric field, *J. Cryst. Growth* 13 (1972) 128–130.
- [47] J. Kim, M.R. Jones, Z. Ou, Q. Chen, In situ electron microscopy imaging and quantitative structural modulation of nanoparticle superlattices, *ACS Nano* 10 (2016) 9801–9808.
- [48] Z. Ou, C. Liu, L. Yao, Q. Chen, Nanoscale cinematography of soft matter system under liquid-phase TEM, *Acc. Mater. Res.* 1 (2020) 41–52.
- [49] J.W. Smith, Q. Chen, Liquid-phase electron microscopy imaging of cellular and biomolecular systems, *J. Mater. Chem. B* 8 (2020) 8490–8506.
- [50] T.H. Moser, H. Mehta, C. Park, R.T. Kelly, T. Shokuhfar, J.E. Evans, The role of electron irradiation history in liquid cell transmission electron microscopy, *Sci. Adv.* 4 (2018) eaaq1202.
- [51] A.C. Varano, A. Rahimi, M.J. Dukes, S. Poelzing, S.M. McDonald, D.F. Kelly, Visualizing virus particle mobility in liquid at the nanoscale, *Chem. Commun.* 51 (2015) 16176–16179.
- [52] J.H. Park, N.M. Schneider, J.M. Grogan, M.C. Reuter, H.H. Bau, S. Kodambaka, F. M. Ross, Control of electron beam-induced Au nanocrystal growth kinetics through solution chemistry, *Nano Lett.* 15 (2015) 5314–5320.
- [53] A.W. Robertson, G. Zhu, B.L. Mehdi, R.M. Jacobs, J. De Yoreo, N.D. Browning, Nanoparticle immobilization for controllable experiments in liquid-cell transmission electron microscopy, *ACS Appl. Mater. Interfaces* 10 (2018) 22801–22808.
- [54] X. Ye, M.R. Jones, L.B. Frechette, Q. Chen, A.S. Powers, P. Ercius, G. Dunn, G. M. Rotskoff, S.C. Nguyen, V.P. Adiga, Single-particle mapping of nonequilibrium nanocrystal transformations, *Science* 354 (2016) 874–877.
- [55] H. Zheng, R.K. Smith, Y.-W. Jun, C. Kisielowski, U. Dahmen, A.P. Alivisatos, Observation of single colloidal platinum nanocrystal growth trajectories, *Science* 324 (2009) 1309–1312.
- [56] G. Lin, S.W. Chee, S. Raj, P. Král, U. Mirsaidov, Linker-mediated self-assembly dynamics of charged nanoparticles, *ACS nano* 10 (2016) 7443–7450.
- [57] S.W. Chee, U. Anand, G. Bisht, S.F. Tan, U. Mirsaidov, Direct observations of the rotation and translation of anisotropic nanoparticles adsorbed at a liquid–solid interface, *Nano Lett.* 19 (2019) 2871–2878.
- [58] S.W. Chee, Z. Baraissov, N.D. Loh, P.T. Matsudaira, U. Mirsaidov, Desorption-mediated motion of nanoparticles at the liquid–solid interface, *J. Phys. Chem. C* 120 (2016) 20462–20470.
- [59] Y. Liu, X.M. Lin, Y. Sun, T. Rajh, In situ visualization of self-assembly of charged gold nanoparticles, *J. Am. Chem. Soc.* 135 (2013) 3764–3767.
- [60] A. Verch, M. Pfaff, N. de Jonge, Exceptionally slow movement of gold nanoparticles at a solid/liquid interface investigated by scanning transmission electron microscopy, *Langmuir* 31 (2015) 6956–6964.

- [61] C. Liu, Z. Ou, F. Guo, B. Luo, W. Chen, L. Qi, Q. Chen, "Colloid-Atom Duality" in the assembly dynamics of concave gold nanoarrows, *J. Am. Chem. Soc.* 142 (2020) 11669–11673.
- [62] J. Park, H. Zheng, W.C. Lee, P.L. Geissler, E. Rabani, A.P. Alivisatos, Direct observation of nanoparticle superlattice formation by using liquid cell transmission electron microscopy, *ACS Nano* 6 (2012) 2078–2085.
- [63] A.S. Powers, H.G. Liao, S.N. Raja, N.D. Bronstein, A.P. Alivisatos, H. Zheng, Tracking nanoparticle diffusion and interaction during self-assembly in a liquid cell, *Nano Lett.* 17 (2017) 15–20.
- [64] E. Cepeda-Perez, D. Doblas, T. Kraus, N. de Jonge, Electron microscopy of nanoparticle superlattice formation at a solid-liquid interface in nonpolar liquids, *Sci. Adv.* 6 (2020) eaba1404.
- [65] B. Luo, J.W. Smith, Z. Ou, Q. Chen, Quantifying the self-assembly behavior of anisotropic nanoparticles using liquid-phase transmission electron microscopy, *Acc. Chem. Res.* 50 (2017) 1125–1133.
- [66] D. Lee, H. Park, Y. Ko, H. Park, T. Hyeon, K. Kang, J. Park, Direct observation of redox mediator-assisted solution-phase discharging of Li–O₂ battery by liquid-phase transmission electron microscopy, *J. Am. Chem. Soc.* 141 (2019) 8047–8052.
- [67] H. Rullgård, L.G. Öfverstedt, S. Masich, B. Daneholt, O. Öktem, Simulation of transmission electron microscope images of biological specimens, *J. Microsc.* 243 (2011) 234–256.
- [68] D.S. Kermany, M. Goldbaum, W. Cai, C.C. Valentim, H. Liang, S.L. Baxter, A. McKeown, G. Yang, X. Wu, F. Yan, Identifying medical diagnoses and treatable diseases by image-based deep learning, *Cell* 172 (2018) 1122–1131, e1129.
- [69] T.-D. Do, M.-T. Duong, Q.-V. Dang, M.-H. Le, Real-time self-driving car navigation using deep neural network, in: 2018 4th International Conference on Green Technology and Sustainable Development (GTSD), IEEE, 2018, pp. 7–12.
- [70] Y. Taigman, M. Yang, M.A. Ranzato, L. Wolf, Deepface: closing the gap to human-level performance in face verification, in: Proceedings of the IEEE Conference on Computer Vision and Pattern Recognition, 2014, pp. 1701–1708.
- [71] L. Yao, Z. Ou, B. Luo, C. Xu, Q. Chen, Machine learning to reveal nanoparticle dynamics from liquid-phase TEM videos, *ACS Cent. Sci.* 6 (2020) 1421–1430.
- [72] O. Ronneberger, P. Fischer, T. Brox, U-net: convolutional networks for biomedical image segmentation, in: International Conference on Medical Image Computing and Computer-assisted Intervention, Springer, 2015, pp. 234–241.
- [73] M.H. Nielsen, S. Aloni, J.J. De Yoreo, In situ TEM imaging of CaCO₃ nucleation reveals coexistence of direct and indirect pathways, *Science* 345 (2014) 1158–1162.
- [74] K. Binder, Theory of first-order phase transitions, *Rep. Prog. Phys.* 50 (1987) 783.
- [75] S. Karthika, T.K. Radhakrishnan, P. Kalaiichelvi, A review of classical and nonclassical nucleation theories, *Cryst. Growth Des.* 16 (2016) 6663–6681.
- [76] G. Lin, S.W. Chee, S. Raj, P. Kral, U. Mirsaidov, Linker-mediated self-assembly dynamics of charged nanoparticles, *ACS Nano* 10 (2016) 7443–7450.
- [77] J. Lee, E. Nakouzi, M. Song, B. Wang, J. Chun, D. Li, Mechanistic understanding of the growth kinetics and dynamics of nanoparticle superlattices by coupling interparticle forces from real-time measurements, *ACS Nano* 12 (2018) 12778–12787.
- [78] Q. Chen, H. Cho, K. Manthiram, M. Yoshida, X. Ye, A.P. Alivisatos, Interaction potentials of anisotropic nanocrystals from the trajectory sampling of particle motion using in situ liquid phase transmission electron microscopy, *ACS Cent. Sci.* 1 (2015) 33–39.
- [79] Y. Wang, X. Peng, A. Abelson, P. Xiao, C. Qian, L. Yu, C. Ophus, P. Ercius, L. W. Wang, M. Law, H. Zheng, Dynamic deformability of individual PbSe nanocrystals during superlattice phase transitions, *Sci. Adv.* 5 (2019) eaaw5623.
- [80] W.C. Lee, B.H. Kim, S. Choi, S. Takeuchi, J. Park, Liquid cell electron microscopy of nanoparticle self-assembly driven by solvent drying, *J Phys Chem Lett* 8 (2017) 647–654.
- [81] Q. Chen, J.M. Yuk, M.R. Hauwiller, J. Park, K.S. Dae, J.S. Kim, A.P. Alivisatos, Nucleation, growth, and superlattice formation of nanocrystals observed in liquid cell transmission electron microscopy, *MRS Bull.* 45 (2020) 713–726.
- [82] B.H. Kim, J. Yang, D. Lee, B.K. Choi, T. Hyeon, J. Park, Liquid-phase transmission electron microscopy for studying colloidal inorganic nanoparticles, *Adv. Mater.* 30 (2018) 1703316.
- [83] J.F. Lutsko, G. Nocolis, Theoretical evidence for a dense fluid precursor to crystallization, *Phys. Rev. Lett.* 96 (2006) 046102.
- [84] A. Sauter, F. Roosen-Runge, F. Zhang, G. Lotze, A. Feoktystov, R.M. Jacobs, F. Schreiber, On the question of two-step nucleation in protein crystallization, *Faraday Discuss.* 179 (2015) 41–58.
- [85] Y. Zhong, V.R. Allen, J. Chen, Y. Wang, X. Ye, Multistep crystallization of dynamic nanoparticle superlattices in nonaqueous solutions, *J. Am. Chem. Soc.* 144 (2022) 14915–14922.
- [86] M.B. Ross, J.C. Ku, V.M. Vaccarella, G.C. Schatz, C.A. Mirkin, Nanoscale form dictates mesoscale function in plasmonic DNA–nanoparticle superlattices, *Nat. Nanotechnol.* 10 (2015) 453–458.
- [87] D.J. Park, C. Zhang, J.C. Ku, Y. Zhou, G.C. Schatz, C.A. Mirkin, Plasmonic photonic crystals realized through DNA-programmable assembly, *Proc. Natl. Acad. Sci.* 112 (2015) 977–981.
- [88] J. Lim, K. Hippalgaonkar, S.C. Andrews, A. Majumdar, P. Yang, Quantifying surface roughness effects on phonon transport in silicon nanowires, *Nano Lett.* 12 (2012) 2475–2482.
- [89] A. Singh, M. Ferri, M. Tamplenizza, F. Borghi, G. Divitini, C. Ducati, C. Lenardi, C. Piazzoni, M. Merlini, A. Podestà, Bottom-up engineering of the surface roughness of nanostructured cubic zirconia to control cell adhesion, *Nanotechnology* 23 (2012) 475101.
- [90] A. Chernov, J. De Yoreo, L. Rashkovich, P. Vekilov, Step and kink dynamics in inorganic and protein crystallization, *MRS Bull.* 29 (2004) 927–934.
- [91] G.D. Barmparis, Z. Lodziana, N. Lopez, I.N. Remediakis, Nanoparticle shapes by using Wulff constructions and first-principles calculations, *Beilstein J. Nanotechnol.* 6 (2015) 361–368.
- [92] E. Auyeung, T.I. Li, A.J. Senesi, A.L. Schmucker, B.C. Pals, M.O. de La Cruz, C. A. Mirkin, DNA-mediated nanoparticle crystallization into Wulff polyhedra, *Nature* 505 (2014) 73–77.
- [93] Z. Ou, L. Yao, H. An, B. Shen, Q. Chen, Imaging how thermal capillary waves and anisotropic interfacial stiffness shape nanoparticle supracrystals, *Nat. Commun.* 11 (2020) 4555.
- [94] D. Haubold, A. Reichhelm, A. Weiz, L. Borchardt, C. Ziegler, L. Bahrig, S. Kaskel, M. Ruck, A. Eychemüller, The formation and morphology of nanoparticle supracrystals, *Adv. Funct. Mater.* 26 (2016) 4890–4895.
- [95] M.N. O'Brien, H.-X. Lin, M. Girard, M. Olvera de la Cruz, C.A. Mirkin, Programming colloidal crystal habit with anisotropic nanoparticle building blocks and DNA bonds, *J. Am. Chem. Soc.* 138 (2016) 14562–14565.
- [96] M. Liao, X. Xiao, S.T. Chui, Y. Han, Grain-boundary roughening in colloidal crystals, *Phys. Rev. X* 8 (2018) 021045.
- [97] J. Hernández-Guzmán, E.R. Weeks, The equilibrium intrinsic crystal–liquid interface of colloids, *Proc. Natl. Acad. Sci.* 106 (2009) 15198–15202.
- [98] E. Hilou, D. Du, S. Kuei, S.L. Biswal, Interfacial energetics of two-dimensional colloidal clusters generated with a tunable anharmonic interaction potential, *Phys. Rev. Mater.* 2 (2018) 025602.
- [99] J. Hoyt, Z. Trautt, M. Upmanyu, Fluctuations in molecular dynamics simulations, *Math. Comput. Simul.* 80 (2010) 1382–1392.
- [100] J. Hoyt, M. Asta, A. Karma, Method for computing the anisotropy of the solid-liquid interfacial free energy, *Phys. Rev. Lett.* 86 (2001) 5530.
- [101] T. Zykova-Timan, R.E. Rozas, J. Horbach, K. Binder, Computer simulation studies of finite-size broadening of solid–liquid interfaces: from hard spheres to nickel, *J. Phys.: Condens. Matter* 21 (2009) 464102.
- [102] J. Hoyt, M. Asta, Atomistic computation of liquid diffusivity, solid-liquid interfacial free energy, and kinetic coefficient in Au and Ag, *Phys. Rev. B* 65 (2002) 214106.
- [103] K.-Y. Niu, H.-G. Liao, H. Zheng, Visualization of the coalescence of bismuth nanoparticles, *Microsc. Microanal.* 20 (2014) 416–424.
- [104] G. Kuczynski, Study of the sintering of glass, *J. Appl. Phys.* 20 (1949) 1160–1163.
- [105] W.W. Mullins, Theory of thermal grooving, *J. Appl. Phys.* 28 (1957) 333–339.
- [106] F. Nichols, W. Mullins, Morphological changes of a surface of revolution due to capillarity-induced surface diffusion, *J. Appl. Phys.* 36 (1965) 1826–1835.
- [107] Z. Mohamed-Kassim, E.K. Longmire, Drop coalescence through a liquid/liquid interface, *Phys. Fluids* 16 (2004) 2170–2181.
- [108] T.J. Woehl, K.L. Jungjohann, J.E. Evans, I. Arslan, W.D. Ristenpart, N. D. Browning, Experimental procedures to mitigate electron beam induced artifacts during in situ fluid imaging of nanomaterials, *Ultramicroscopy* 127 (2013) 53–63.
- [109] T.U. Dissanayake, M. Wang, T.J. Woehl, Revealing reactions between the electron beam and nanoparticle capping ligands with correlative fluorescence and liquid-phase electron microscopy, *ACS Appl. Mater. Interfaces* 13 (2021) 37553–37562.
- [110] J. Palacci, S. Sacanna, A.P. Steinberg, D.J. Pine, P.M. Chaikin, Living crystals of light-activated colloidal surfers, *Science* 339 (2013) 936–940.
- [111] J. Yan, M. Han, J. Zhang, C. Xu, E. Luijten, S. Granick, Reconfiguring active particles by electrostatic imbalance, *Nat. Mater.* 15 (2016) 1095–1099.